Nano Energy 151 (2026) 111815

Contents lists available at ScienceDirect

Nano Energy

journal homepage: www.elsevier.com/locate/nanoen

Full paper

Nanoscale surface roughening enables stable metal–electrolyte interfaces☆

Hongtao Sun, Weiyu Li *

Department of Mechanical Engineering, University of Wisconsin-Madison, Madison, WI 53706, USA

ARTICLE INFO

Keywords:
Li–metal batteries
Dendrite suppression
Phase-field modeling
Morphology evolution
Nanoscale roughness
Defects

ABSTRACT

Unstable lithium (Li) deposition and dendrite formation limit the performance and safety of Li–metal batteries. Although nanoscale surface roughness and intrinsic defects are known to influence interfacial morphology, their coupled roles in nonlinear dendrite evolution remain poorly understood. Here, we employ high-resolution nonlinear electrochemical phase-field simulations with adaptive mesh refinement to systematically investigate how nanoscale roughness wavelength and amplitude, together with defect size and density, govern Li–metal interfacial stability. We find that roughness wavelength emerges as the primary control parameter for interfacial stability. Shorter wavelengths suppress dendrite growth by increasing interfacial energy penalties and altering ion transport, but this effect saturates below a critical wavelength set by roughness amplitude and defect properties. At long wavelengths, increasing amplitude destabilizes the interface, while at short wavelengths stability is maintained even at large amplitudes. Defect effects depend strongly on the background roughness regime. At long wavelengths, moderate defect densities can disrupt background-driven instabilities and reduce dendrite growth, whereas high defect densities or large defects promote localized current focusing and accelerate growth. In contrast, when the background wavelength is stabilizing, dendrite length increases monotonically with defect density. Comparison with linear stability analysis confirms its ability to predict early-time wavelength selection, but also reveals its limitations in capturing the effects of finite-amplitude roughness, defect interactions, and nonlinear coupling between transport and surface energy that govern interfacial evolution at later times. These results demonstrate that nanoscale roughening, beyond simply reducing defects, is an effective and tunable strategy for stabilizing Li–metal interfaces. By coupling nanoscale wavelength, amplitude, and defect statistics, our simulations yield generalizable design rules and provide a predictive framework for engineering Li–metal anodes.

1. Introduction

Lithium-metal batteries (LMBs) offer exceptionally high energy density but remain constrained by unstable metal deposition and the formation of lithium dendrites [1,2]. These dendritic structures can penetrate the separator and trigger internal short circuits, posing severe safety risks and limiting cycle life, particularly under fast-charging conditions [3,4]. The morphology of the lithium (Li)–electrolyte interface governs both the initiation and propagation of dendritic growth [5–8]. Therefore, understanding how to control interfacial morphology and, ultimately, how to suppress or redirect dendrite formation is essential for enabling practical, high-energy-density LMBs.

Extensive experimental efforts have explored electrolyte formulations [9–11], additives [12,13], artificial interphases [14,15], and engineered surface coatings [16,17] to regulate Li deposition morphology. Computational studies at multiple scales have complemented these advances: molecular dynamics simulations clarify the transport and solvation structure of Li-ions and resolve interfacial processes at atomic and molecular length scales [18,19]; mesoscale models such as phase-field frameworks [20–23] and kinetic Monte Carlo approaches [24,25] that capture mesoscale morphological evolution under coupled electro-chemo-mechanical effects [26]; continuum-scale transport and electrochemical models such as the pseudo-two-dimensional models quantify device-level charging–discharging characteristics [27,28]. Linear stability analyses [29,30] provide analytical relationships between surface roughness, interphase properties, and perturbation wavelength, revealing how these factors govern the growth rates of interfacial instabilities.

The nanoscale regime is particularly important for metal anode stability because surface features with wavelengths and amplitudes of tens to hundreds of nanometers directly modulate the electrochemical and mechanical fields that govern dendrite initiation [31–

☆ This article is part of a Special issue entitled: 'Emerging Investigator' published in Nano Energy.

* Corresponding author.
E-mail address: weiyu.li@wisc.edu (W. Li).

https://doi.org/10.1016/j.nanoen.2026.111815
Received 26 December 2025; Received in revised form 10 February 2026; Accepted 17 February 2026
Available online 23 February 2026

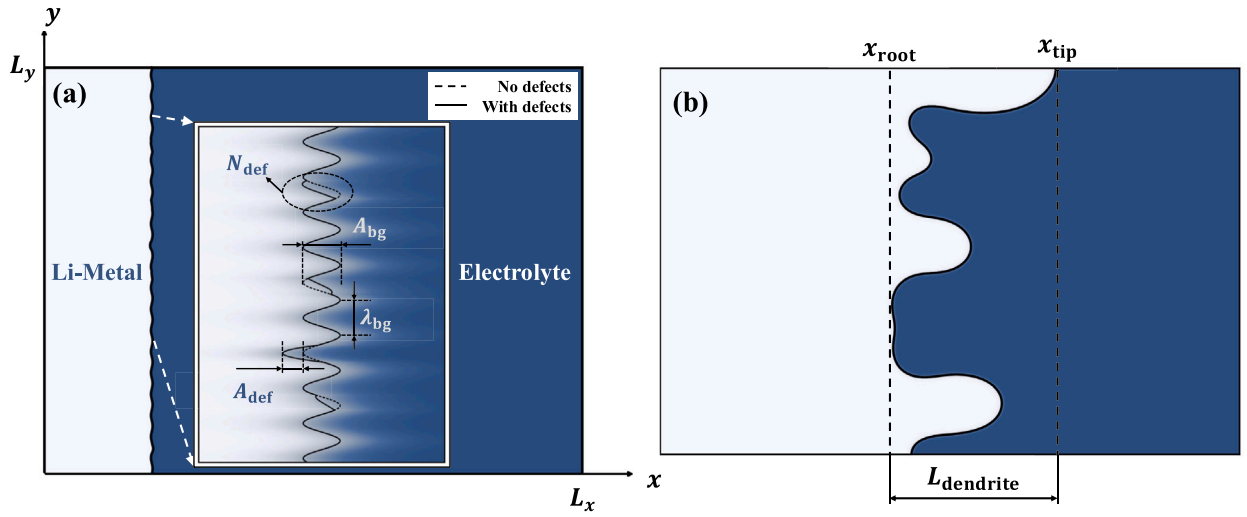

Fig. 1. Schematic illustration of the phase-field simulation setup and dendrite metrics. (a) Computational domain $\Omega = [0, L_x]\times[0, L_y]$, consisting of a Li–metal anode region Ω_s (left, silver) and an electrolyte region Ω_e (right, blue). The magnified inset shows the initial Li–electrolyte interface, which includes both background nanoscale roughness and prescribed surface defects. The dashed line denotes the background roughness alone, while the solid line indicates additional localized defects superimposed on it. Here, A_{bg} and λ_{bg} denote the amplitude and wavelength of the background roughness, A_{def} is the defect amplitude, and N_{def} denotes the number of defects. (b) Definition of dendrite length $L_{dendrite}$, measured as the axial distance from the root position x_{root} to the furthest tip position x_{tip}.

33]. At these length scales, nanoscale curvature alters local charge-transfer kinetics, electric double-layer structure, and ion depletion behavior, thereby influencing the spatial distribution of interfacial current [34,35]. Experimentally, nano-engineered architectures, including patterned substrates [36,37], nanoporous hosts [38,39], and functionalized separators, [40] have demonstrated improved deposition uniformity and reduced flux heterogeneity. These approaches impact nanoscale ion transport, interfacial reaction kinetics, and local mechanical responses, e.g., by increasing the surface-energy penalty for forming sharp protrusions, which together stabilize the interface. Theoretically, nanoscale perturbations correspond to wavelengths at which curvature-induced overpotential variations and SEI transport limitations significantly modify the dendrite growth rates predicted by linear stability theory [29,41]. Computationally, resolving such nanoscale behavior requires capturing steep concentration and overpotential gradients around small asperities and the evolution of ultrathin SEI layers, motivating nonlinear, high-resolution phase-field simulations with adaptive mesh refinement [42–44]. Importantly, nanoscale surface features include not only engineered architectures but also intrinsic defects, such as pits, voids and scratches, that fall within similar wavelength scales and may exert a comparable influence on local transport and interfacial behavior [45,46]. Together, these insights demonstrate that nanoscale morphology is a primary design parameter governing Li–metal interfacial stability.

Despite these advances, several gaps and challenges remain. Linear stability analyses provide insight only in the infinitesimal-perturbation limit and do not capture the nonlinear growth, mode interactions, or long-time morphology changes that arise as nanoscale perturbations amplify. In practical interface engineering, however, surface roughness is deliberately introduced over nanoscale-to-microscale wavelengths and amplitudes as a designed background texture, rather than as an infinitesimal perturbation [32]. Such finite-amplitude, spatially structured roughness lies outside the assumptions of linear theory. In addition, intrinsic defects are still ubiquitous on Li–metal surfaces; the combined effects of defect size, density, spacing, and arrangement on intentionally structured surfaces remain poorly quantified. These limitations make it difficult to assess how nanoscale roughness and defect morphology jointly influence interfacial evolution beyond the linear regime. As a result, existing modeling approaches do not yet provide a systematic way to connect nanoscale geometry (e.g., amplitude, wavelength) and defect characteristics (e.g., size, density, spacing) to their nonlinear evolution during metal deposition, even though such understanding is essential for establishing generalizable design rules for stabilizing metal anodes through nanoscale surface engineering.

In this work, we use nonlinear electrochemical phase-field simulations with adaptive mesh refinement to resolve interfacial dynamics at nanoscale fidelity. We systematically examine how controlled nanoscale surface roughening, i.e., with prescribed perturbation wavelengths and amplitudes, evolves from early- to late-time morphology. We further investigate the role of defects and analyze how defect size and number density influence deposition behavior. By introducing stochastic defect distributions, we assess the competition between intentional nanoscale structuring and unavoidable imperfections. This framework enables us to quantify the transition from linear to nonlinear growth regimes, directly compare nonlinear evolution with predictions from linear stability theory, and elucidate how nanoscale surface features modify local ion transport and electrochemical driving forces near protrusions and valleys. These results provide mechanistic insight into how nanoscale structures and defects jointly govern dendrite initiation and growth, forming the basis for generalizable design principles for stabilizing metal anodes through nanoscale surface engineering (see Fig. 1).

2. Methods

2.1. Problem formulation

Fig. 1 illustrates the phase-field simulation setup and the definition of dendrite metrics. We consider a 2D half-cell consisting of a Li–metal anode and a liquid electrolyte (1 M $LiPF_6$ in EC/DMC, 1:1 by volume). The simulation domain is defined as $\Omega = [0, L_x] \times [0, L_y]$, with spatial coordinate $\mathbf{x} = (x, y)$. We set $L_x = 200$ μm and $L_y = 100$ μm. The boundaries are the left current collector Γ_L (at $x = 0$), the right bulk electrolyte boundary Γ_R (at $x = L_x$), the bottom boundary Γ_B (at $y = 0$), and the top boundary Γ_T (at $y = L_y$). At $t = 0$ s, the Li–metal anode Ω_s has a mean thickness of 20 μm, while the remaining 180 μm is occupied by the electrolyte Ω_l. The initial metal–electrolyte interface is prescribed with a periodic background roughness of amplitude A_{bg} and wavelength λ_{bg}, onto which localized surface defects of amplitude A_{def} are superimposed. The number of such defects is denoted by

N_{def}. This parameterization enables systematic control of both designed roughness and intrinsic defect characteristics. Electrodeposition occurs at the metal–electrolyte interface via the reaction $Li^+ + e^- \rightarrow Li$, which converts Li-ions in the electrolyte into Li–metal at the interface, causing the Li–electrolyte boundary to advance over time. We assume a dilute electrolyte with bulk concentration c_0. We neglect convective transport and impose electroneutrality in the electrolyte, such that the cation and anion concentrations satisfy $c_+(\mathbf{x},t) = c_-(\mathbf{x},t)$ [47]. The dendrite length L_{dendrite} is defined as the axial distance between the root position x_{root} and the furthest tip position x_{tip} along the deposition direction.

To capture the motion of the metal–electrolyte interface during electrodeposition, we employ a phase-field formulation [48] in which a continuous order parameter $\xi(\mathbf{x},t)$ represents a dimensionless Li–metal concentration, with $\xi = 0$ corresponding to the liquid electrolyte phase and $\xi = 1$ corresponding to the metallic lithium phase. These two phases are separated by a diffuse interface of finite thickness, across which the phase-field parameter ξ transitions from 0 to 1 smoothly. The evolution of ξ is determined by interfacial free energy and electrochemical driving forces, which can capture the motion and morphological changes of the interface. We express the Gibbs free energy of the system as [21]

$$G = \int_V \left[f_{\mathrm{ch}}(\mathbf{c}) + f_{\mathrm{grad}}(\nabla \mathbf{c}) + f_{\mathrm{elec}}(\mathbf{c},\phi) \right] dV, \tag{1}$$

where $\mathbf{c} = \{\tilde{c}_s, \tilde{c}_+, \tilde{c}_-\}$ denotes the set of dimensionless concentrations. The normalized Li–metal concentration is defined as $\tilde{c}_s = c_s/C_m^s$, where C_m^s is the site density of Li–metal. The phase-field variable corresponds directly to the solid-phase concentration, i.e., $\tilde{c}_s = \xi$. $f_{\mathrm{ch}}(\mathbf{c}) = g(\xi) + RT(c_+ \ln \hat{c}_+ + c_- \ln \hat{c}_-) + c_+\mu_+^\Theta + c_-\mu_-^\Theta$ denotes the chemical free energy, where $g(\xi)$ is the double-well potential, R and T denote the gas constant and temperature, $\hat{c}_\pm = c_\pm/c^\Theta$, where c^Θ is the standard concentration, and $\mu_\pm^\Theta$ denote the standard chemical potentials. $f_{\mathrm{grad}} = \kappa/2|\nabla\xi|^2$ represents the gradient energy, where κ is the gradient energy coefficient. $f_{\mathrm{elec}} = F(z_+c_+ + z_-c_-)\phi$ is the electrostatic free energy, where ϕ is the electric potential, F is Faraday's constant, and z_+ and z_- are ionic charge numbers. The interfacial free energy is defined as [49]

$$G_{\mathrm{int}} = \int_V \left[g(\xi) + \frac{\kappa}{2} |\nabla\xi|^2 \right] dV, \tag{2}$$

where $g(\xi) = W\xi^2(1-\xi)$ and W is the barrier height. The parameters W and κ are linked to physical interface properties by $W = 3\gamma/D$ and $\kappa = 6\gamma D$, where γ represents the interfacial tension and D is the interface thickness.

To determine the evolution of ξ, we adopt the standard variational framework of phase-field theory. Without external work, the system is assumed to evolve to decrease its total free energy. Consequently, the contribution of interfacial free energy to the evolution of the phase-field parameter is given by the functional derivative of G_{int} with respect to ξ. Under this assumption, the interfacial phase-field kinetics is written in Allen–Cahn form as [50]

$$\left.\frac{\partial\xi}{\partial t}\right|_{\mathrm{int}} = -\mathcal{L}_\sigma \frac{\delta G_{\mathrm{int}}}{\delta\xi} = -\mathcal{L}_\sigma \left[g'(\xi) - \kappa\nabla^2\xi \right], \tag{3}$$

where $\mathcal{L}_\sigma$ denotes the interfacial mobility. This gradient-flow form ensures that, in the absence of electrochemical reactions and other external driving forces, the interfacial free energy decreases with time, i.e., $\mathrm{d}G_{\mathrm{int}}/\mathrm{d}t \le 0$, thus allowing the system to spontaneously relax towards a local minimum of G_{int}. The morphological evolution of the interface is also driven by the electrochemical reaction, which is governed by Butler–Volmer kinetics. The reaction-induced contribution to the phase-field evolution equation is expressed by [51]

$$\left.\frac{\partial\xi}{\partial t}\right|_{\mathrm{e}} = -\mathcal{L}_\eta\, h'(\xi) \left[\exp\left(\frac{(1-\alpha)nF\eta_\alpha}{RT} \right) - \hat{c}_+ \exp\left(-\frac{\alpha nF\eta_\alpha}{RT} \right) \right], \tag{4}$$

where $\mathcal{L}_\eta$ is electrochemical reaction coefficient; n is the number of electrons transferred; α is the charge transfer coefficient; $\eta_\alpha = \phi_a - \phi - E^\theta$ is the activation overpotential, where ϕ_a is the applied potential, ϕ is the electric potential in the electrolyte and Li metal, and E^θ is the equilibrium half-cell potential. To localize the reaction within the diffuse metal–electrolyte interface, we employ a smooth interpolation function $h(\xi) = \xi^3(6\xi^2 - 15\xi + 10)$, which satisfies $h(0) = 0$ in the electrolyte and $h(1) = 1$ in the solid electrode. Its derivative $h'(\xi)$ is nonzero only within the interfacial region and therefore weights the electrochemical source term in the phase-field dynamics.

Combining the interfacial and electrochemical reaction terms in Eqs. (3) and (4) yields the phase-field evolution equation for $\xi(\mathbf{x},t)$ [21],

$$\frac{\partial\xi}{\partial t} = -\mathcal{L}_\sigma \left(g'(\xi) - \kappa\nabla^2\xi \right) - \mathcal{L}_\eta h'(\xi) \times \left[\exp\left(\frac{(1-\alpha)nF\eta_\alpha}{RT} \right) - \hat{c}_+ \exp\left(-\frac{\alpha nF\eta_\alpha}{RT} \right) \right], \tag{5}$$

where the first term on the right-hand side describes the competition between bulk free-energy driving forces that promote phase separation and interfacial energy that penalizes curvature. The second term represents the nonlinear electrochemical driving force arising from charge transfer reactions within the diffuse interfacial region.

The Li chemical potential field $\mu(\mathbf{x},t)$ evolves according to a modified diffusion equation that incorporates diffusion, electro-migration, and the redistribution of Li species between phases [20],

$$\chi\frac{\partial\mu}{\partial t} = \nabla\cdot\left[D_l(1-h(\xi))^2 \frac{c_+}{RT}(\nabla\mu + nF\nabla\phi) \right] - \frac{\partial h(\xi)}{\partial t}\left(C_m^s\theta(\mu;\mathcal{E}_s) - C_m^l\theta(\mu;\mathcal{E}_l) \right) \tag{6}$$

where D_l is the Li-ion diffusion coefficient in the electrolyte, modulated by the factor $(1-h(\xi))^2$. This penalization enforces vanishing ionic diffusivity in the metallic phase ($\xi \rightarrow 1$) and ensures that mass transport occurs exclusively within the electrolyte, while preserving a smooth transition across the diffuse interface. C_m^l is the site density of Li-ions in the electrolyte; $\theta(\mu;\mathcal{E}_\beta)$, with $\beta \in \{s,l\}$, denotes the site-occupancy function in the solid and liquid phases, respectively. It is expressed in lattice-gas (Fermi–Dirac) form as $\theta(\mu;\mathcal{E}_\beta) = \exp\left(\frac{\mu-\mathcal{E}_\beta}{RT}\right)/[1+\exp\left(\frac{\mu-\mathcal{E}_\beta}{RT}\right)]$, which gives the fraction of available lattice sites occupied by Li as a function of the local chemical potential μ. The prefactor χ is

$$\chi = \frac{\partial\theta(\mu;\mathcal{E}_s)}{\partial\mu}C_m^s h(\xi) + \frac{\partial\theta(\mu;\mathcal{E}_l)}{\partial\mu}C_m^l(1-h(\xi)). \tag{7}$$

The Li-ion concentration in the electrolyte is [20]

$$c_+(\mu) = C_m^l\theta(\mu;\mathcal{E}_l)(1-h(\xi)), \tag{8}$$

The parameter $\mathcal{E}_\beta$ represents the reference chemical-potential offset for Li occupation in phase $\beta \in \{s,l\}$. It sets the energetic baseline of the lattice-gas occupancy relation in each phase and is determined by enforcing thermodynamic equilibrium between the chemical potential μ and the prescribed equilibrium Li concentration in that phase. Specifically,

$$\mathcal{E}_\beta = \mu_0 - RT\ln\left(\frac{c_0^\beta}{C_m^\beta - c_0^\beta} \right), \tag{9}$$

where c_0^β is the initial equilibrium Li concentration. Without loss of generality, we set the reference equilibrium chemical potential $\mu_0 = 0$. In the solid phase, the equilibrium Li occupancy is taken to be nearly complete, and we prescribe $c_0^s = (1-\delta)C_m^s$ with $\delta = 10^{-6}$ to avoid numerical singularity. In the electrolyte phase, c_0^l is set to the bulk electrolyte concentration.

Charge conservation in the electrolyte is described by a Poisson-type equation. The divergence of the ionic current is balanced by the volumetric source term representing the net charge consumed or released by the Faradaic reaction within the diffuse interface [21],

$$\nabla\cdot(\sigma_{\mathrm{eff}}\nabla\phi) = nFC_m^s\frac{\partial\xi}{\partial t}, \tag{10}$$

where $\sigma_{\mathrm{eff}}(\xi) = \sigma_e\, h(\xi) + \sigma_l\,[1-h(\xi)]$ is the effective conductivity that related to the conductivity of electrode σ_s and electrolyte σ_l.

2.1.1. Boundary and initial conditions

The problem is solved for a vector of three unknown fields, $\mathbf{u} = (\xi, \mu, \phi)$, corresponding to the phase-field order parameter, the electrolyte chemical potential, and the electric potential. The boundary conditions for ξ, μ, and ϕ are prescribed on the left current-collector boundary Γ_L, the right electrolyte boundary Γ_R, and the top and bottom boundaries Γ_T and Γ_B. These boundaries correspond to $\Gamma_L = \{x = 0,\ 0 \le y \le L_y\}$, $\Gamma_R = \{x = L_x,\ 0 \le y \le L_y\}$, $\Gamma_B = \{y = 0,\ 0 \le x \le L_x\}$, and $\Gamma_T = \{y = L_y,\ 0 \le x \le L_x\}$.

Phase-field order parameter ξ. Dirichlet boundary conditions are imposed on the left and right boundaries to fix the solid and electrolyte phases, respectively, while zero-flux conditions are applied on the top and bottom boundaries,

$$\xi(0, y, t) = 1, \qquad \xi(L_x, y, t) = 0, \qquad \frac{\partial \xi}{\partial y} = 0 \quad \text{for } y = 0 \text{ and } y = L_y. \tag{11}$$

Chemical potential μ. The chemical potential is fixed at the right boundary to represent the bulk electrolyte reference state, while zero-flux conditions are imposed on the remaining boundaries,

$$\mu(L_x, y, t) = 0, \qquad \frac{\partial \mu}{\partial x} = 0 \quad \text{for } x = 0,$$
$$\frac{\partial \mu}{\partial y} = 0 \quad \text{for } y = 0 \text{ and } y = L_y. \tag{12}$$

Electric potential ϕ. An externally applied potential ϕ_a is prescribed at the current collector, and the electrolyte boundary is grounded. Zero-flux conditions are applied on the top and bottom boundaries,

$$\phi(0, y, t) = \phi_a, \qquad \phi(L_x, y, t) = 0, \qquad \frac{\partial \phi}{\partial y} = 0 \quad \text{for } y = 0 \text{ and } y = L_y. \tag{13}$$

The system is initialized with a diffuse metal–electrolyte interface at $x_0 = 20$ μm, onto which controlled transverse perturbations $\delta(y)$ are imposed. The phase-field profile is initialized using a hyperbolic tangent function,

$$\xi(\mathbf{x}, 0) = \frac{1}{2}\left[1 - \tanh\left(\zeta\left[x - x_0 + \delta(y)\right]\right)\right], \tag{14}$$

where ζ controls the diffuse-interface thickness. The perturbation field $\delta(y)$ is constructed as the superposition of a background roughness profile and a set of localized interfacial defects, $\delta(y) = \delta_{bg}(y) + \delta_{def}(y)$. The background roughness $\delta_{bg}(y)$ introduces a controlled, periodic nanoscale modulation of the interface [29],

$$\delta_{bg}(y) = A_{bg} \sin\left(\frac{2\pi y}{\lambda_{bg}}\right), \tag{15}$$

where A_{bg} is the roughness amplitude and λ_{bg} is the roughness wavelength, which can be related through the number of complete waves across the domain height, $\lambda_{bg} = L_y / N_{bg}$.

Real solid-state interfaces simultaneously contain multiple defect types (including voids, grain boundaries, and impurities) [52]. To reflect this inherent variability, we model defects as stochastic perturbations with randomized locations and amplitudes, thereby quantifying the statistical impact of the defect set on dendrite growth. Specifically, localized surface defects are represented by the defect field $\delta_{def}(y)$, which models discrete morphological irregularities superimposed on the background roughness,

$$\delta_{def}(y) = \sum_{i=1}^{N_{def}} s_i \cdot \alpha_i \cdot A_{def} \cdot \hat{f}_{cap}(y - y_i; R), \tag{16}$$

where N_{def} is the number of defects, $s_i \in \{-1, +1\}$ is randomly assigned with equal probability to represent depressions (-1) and protrusions ($+1$), α_i is a random scaling factor drawn from a uniform distribution to introduce size variability, A_{def} is the nominal defect amplitude, and y_i is the randomly assigned location of defect i. The normalized shape function $\hat{f}_{cap}(y; R)$ defines a spherical-cap profile with characteristic radius R. A fixed random seed is used to ensure reproducibility.

By varying the background wavelength λ_{bg}, background amplitude A_{bg}, defect number N_{def}, and defect amplitude A_{def}, the initial nanoscale interface morphology is systematically controlled. This formulation enables quantitative investigation of how nanoscale roughness and intrinsic defects jointly influence Li electrodeposition stability and dendrite growth suppression.

The chemical potential field is initialized in a manner consistent with the diffuse metal–electrolyte interface by coupling it to the phase-field variable,

$$\mu(\mathbf{x}, 0) = -10\, RT\, \xi(\mathbf{x}, 0). \tag{17}$$

This initialization yields an initial chemical potential of approximately $-10RT$ within the lithium metal ($\xi \approx 1$) and 0 in the electrolyte ($\xi \approx 0$), with a smooth transition across the diffuse interface. This initialization ensures that the chemical potential field is thermodynamically consistent with the phase-field variable. The electric potential field is initialized analogously to ensure a consistent electrochemical state,

$$\phi(\mathbf{x}, 0) = \phi_a\, \xi(\mathbf{x}, 0), \tag{18}$$

providing an initial electric potential of ϕ_a within the solid anode and 0 V in the electrolyte, with a continuous potential drop across the diffuse interface.

2.1.2. Normalization

To nondimensionalize the governing equations, we introduce the characteristic length $L_0 = 1$ μm, time scale $\tau_0 = 1.0$ s, and reference conductivity $\sigma_{ref} = 1\ \mathrm{S\ m^{-1}}$. The corresponding dimensionless variables are defined as

$$\tilde{\mathbf{x}} = \frac{\mathbf{x}}{L_0}, \quad \tilde{t} = \frac{t}{\tau_0}, \quad \tilde{\mu} = \frac{\mu}{RT}, \quad \tilde{\phi} = \frac{\phi F}{RT}, \quad \tilde{c}_+ = \frac{c_+}{c_0}. \tag{19}$$

Under this normalization, the phase-field evolution equation becomes

$$\frac{\partial \xi}{\partial \tilde{t}} = -\tilde{\mathcal{L}}_\sigma\left[\tilde{g}'(\xi) - \tilde{\kappa}\tilde{\nabla}^2\xi\right] - \tilde{\mathcal{L}}_\eta h'(\xi)\left[e^{(1-\alpha)n\tilde{\phi}} - \tilde{c}_+(\tilde{\mu})\frac{c_0}{c^\Theta}e^{-\alpha n\tilde{\phi}}\right] \tag{20}$$

where $\tilde{\mathcal{L}}_\sigma$ and $\tilde{\mathcal{L}}_\eta$ are the dimensionless mobility coefficients associated with interfacial relaxation and electrochemical reaction kinetics, respectively. The dimensionless chemical free-energy density is defined as $\tilde{g}(\xi) = \tilde{W}\,\xi^2(1-\xi)$, where $\tilde{W}$ is the normalized double-well barrier height. The interfacial energy parameters satisfy $\tilde{W} = 3\tilde{\gamma}/\tilde{D}$, $\tilde{\kappa} = 6\tilde{\gamma}\,\tilde{D}$, with $\tilde{\gamma}$ denoting the dimensionless interfacial tension and $\tilde{D}$ the dimensionless diffuse-interface thickness. Details of the normalization and numerical values of these parameters are summarized in Table 1. The reference chemical-potential offsets are likewise nondimensionalized as $\tilde{\mathcal{E}}_\beta = \mathcal{E}_\beta/(RT)$, with $\beta \in \{s, l\}$.

The dimensionless chemical potential equation is given by

$$\tilde{\chi}\frac{\partial \tilde{\mu}}{\partial \tilde{t}} = \tilde{\nabla}\cdot\left[\tilde{D}_l(1-h(\xi))^2\frac{\tilde{c}_+(\tilde{\mu})}{\tilde{C}_m^l}\left(\tilde{\nabla}\tilde{\mu} + \tilde{\nabla}\tilde{\phi}\right)\right]$$
$$-\frac{\partial h(\xi)}{\partial \tilde{t}}\left(\frac{C_m^s}{C_m^l}\theta(\tilde{\mu}; \tilde{\mathcal{E}}_s) - \theta(\tilde{\mu}; \tilde{\mathcal{E}}_l)\right), \tag{21}$$

where $\tilde{D}_l = D_l\tau_0/L_0^2$ is the dimensionless Li-ion diffusion coefficient in the electrolyte. The normalized thermodynamic susceptibility is defined as $\tilde{\chi} = \chi/C_m^l$.

The nondimensional governing equation for the electric potential is

$$\tilde{\nabla}\cdot\left(\tilde{\sigma}\,\tilde{\nabla}\tilde{\phi}\right) = C\frac{\partial \xi}{\partial \tilde{t}}, \tag{22}$$

where $\tilde{\sigma} = \sigma/\sigma_{ref}$ is the normalized conductivity and $C = nF^2C_m^s L_0^2/(\sigma_{ref}\tau_0 RT)$ is a dimensionless coupling parameter characterizing interfacial charge transfer.

The interplay between interfacial energy penalties, electrochemical driving forces, and ion-transport limitations constitutes a general physical mechanism governing metal electrodeposition. As a result,

Table 1
Physical parameters, normalization scales, and corresponding nondimensional values used in the simulations [20].

Parameter	Symbol	Real value	Normalized formula	Normalized value
Interfacial mobility	$\mathcal{L}_\sigma$	2.5×10^{-6} $m^3\,J^{-1}\,s^{-1}$	$\tilde{\mathcal{L}}_\sigma = \mathcal{L}_\sigma c_0 RT\tau_0$	6.25
Reaction constant	$\mathcal{L}_\eta$	1.0×10^{-3} s^{-1}	$\tilde{\mathcal{L}}_\eta = \mathcal{L}_\eta \tau_0$	1.0×10^{-3}
Interfacial energy	γ	0.556 $J\,m^{-2}$	$\tilde{\gamma} = \gamma/(c_0 RT L_0)$	0.22
Interface thickness	D	1 μm	$\tilde{D} = D/L_0$	1.0
Diffusion coefficient in electrolyte	D_l	3.179×10^{-10} $m^2\,s^{-1}$	$\tilde{D}_l = D_l\tau_0/L_0^2$	317.9
Conductivity in electrode	σ_s	1.0×10^{6} $S\,m^{-1}$	$\tilde{\sigma}_s = \sigma_s/\sigma_{ref}$	10^6
Conductivity in electrolyte	σ_l	1.19 $S\,m^{-1}$	$\tilde{\sigma}_l = \sigma_l/\sigma_{ref}$	1.19
Site density of electrode	C_m^s	7.64×10^{4} $mol\,m^{-3}$	$\tilde{C}_m^s = C_m^s/c_0$	76.4
Site density of electrolyte	C_m^l	1.44×10^{4} $mol\,m^{-3}$	$\tilde{C}_m^l = C_m^l/c_0$	14.4
Transfer coefficient	α	0.5	–	0.5

the qualitative design principles identified here are broadly applicable across different metal–electrolyte systems and operating conditions, including variations in temperature and applied potential. Quantitative predictions, however, require material-specific parameters such as ionic diffusivity, electrical conductivity, and electrode site density. The present phase-field framework can be readily extended to other material systems by updating these parameters, as summarized in Table 1, to reflect the properties of the electrolyte and electrode of interest.

2.1.3. Adaptive numerical framework

To accurately resolve the evolving metal–electrolyte interface while maintaining computational efficiency, we employ a fully adaptive numerical framework that combines adaptive mesh refinement with adaptive time stepping. This strategy concentrates spatial and temporal resolution where it is most needed—near the moving reaction front—while avoiding unnecessary refinement in the bulk phases.

Adaptive mesh refinement. The phase-field formulation introduces a diffuse interface of finite width D, across which the order parameter ξ transitions smoothly from 0 (electrolyte) to 1 (metal). Resolving this interfacial region is essential for accurately capturing interface motion and morphological evolution. Because the electrolyte domain size satisfies $L \gg D$, a uniformly refined mesh would be computationally prohibitive. We therefore implement a dynamic adaptive mesh refinement strategy that localizes resolution near the interface using a hierarchical, marker-based approach.

Marking criterion: Cells are marked for refinement or coarsening based on the magnitude of the phase-field gradient, $\nabla\xi$. Cells satisfying $|\nabla\xi| > \epsilon_{\text{refine}}$ are identified as part of the diffuse interface and refined to the finest resolution level $\ell_{\max}$, ensuring that the interface is always fully resolved. Regions with small gradients, corresponding to bulk electrolyte or solid metal, are marked for coarsening.

Refinement and coarsening strategy: Marked cells are refined using a hierarchical, nonconforming refinement scheme, producing a graded mesh that concentrates resolution near the diffuse interface. Rather than performing repeated local coarsening operations, we adopt a global reconstruction strategy to maintain mesh quality over long simulation times. Specifically, when the number of cells marked for coarsening exceeds a prescribed threshold N_{coarse}, the current adaptive mesh is discarded and the mesh is reset to the base level ℓ_0. A new adaptive mesh is then constructed by reapplying the refinement criteria based on the current solution fields. This rollback-and-refine procedure avoids mesh degradation caused by repeated local refinement and coarsening and ensures consistent resolution of the moving interface.

Solution transfer: During mesh adaptation, the solution fields $\mathbf{u} = \{\xi, \tilde{\mu}, \tilde{\phi}\}$ are transferred between meshes using a single projection step. Intermediate meshes generated during the refinement process are used only to evaluate refinement and coarsening criteria and do not carry updated solution fields. The solution is projected only after the final adaptive mesh configuration has been fully constructed, thereby avoiding the accumulation of interpolation errors associated with successive mesh transfers. Conservation of mass and electrochemical energy is monitored during projection to ensure numerical accuracy.

Adaptive time stepping. To ensure the convergence of the nonlinear Newton solver and maintain temporal accuracy, we employ a heuristic adaptive time stepping algorithm. The time step size, Δt, is dynamically adjusted based on the computational difficulty of the previous step, quantified by the number of linear iterations (N_{iter}) required for convergence. It enforces smaller time steps during the initial transient stage, where steep gradients and rapid interfacial evolution demand enhanced stability. Besides, it preserves time accuracy throughout the simulation by reducing Δt when the nonlinear residual becomes stiff. When the solution evolves smoothly and the Newton iterations converge rapidly, the algorithm increases Δt to accelerate the overall computation. This adaptive mechanism balances stability, accuracy, and efficiency across all stages of the simulation.

The time-step update follows a feedback control law,

$$\Delta t_{n+1} = \begin{cases} \min(\Delta t_n \cdot \gamma_{\text{inc}}, \Delta t_{\max}) & \text{if } N_{\text{iter}} < N_{\text{low}}, \\ \max(\Delta t_n \cdot \gamma_{\text{dec}}, \Delta t_{\min}) & \text{if } N_{\text{iter}} > N_{\text{high}}, \\ \Delta t_n & \text{otherwise}, \end{cases} \tag{23}$$

where $\gamma_{\text{inc}} > 1$ and $\gamma_{\text{dec}} < 1$ are growth and damping factors, respectively. N_{low} and N_{high} define the optimal window for solver performance (typically 4–6 iterations). To maintain robustness during the initial transient stage, a smaller maximum time step $\Delta t_{\max}^{\text{early}}$ is enforced.

At each time step, we solve the coupled nonlinear system $\mathbf{u} = \{\xi, \tilde{\mu}, \tilde{\phi}\}$ monolithically using a fully implicit Newton's method with convergence tolerances atol = 10^{-6}, rtol = 10^{-6} and a maximum of 100 iterations. The finite-element discretization and nonlinear solves are implemented using the open-source FEniCS framework [53]. Each Newton step employs a direct LU solver (MUMPS) with tight linear tolerances (rtol = 10^{-8}, atol = 10^{-10}) to ensure linearization errors remain negligible relative to the nonlinear residual.

3. Results and discussion

We numerically solve the coupled, dimensionless governing equations (Eqs. (20)–(22)) together with the prescribed initial and boundary conditions to obtain the spatiotemporal evolution of the phase-field order parameter ξ, the electrochemical potential μ, and the electric potential ϕ. To quantify how initial surface morphology influences Li electrodeposition stability, we vary the background roughness amplitude and wavelength (A_{bg}, λ_{bg}) as well as the defect amplitude and number (A_{def}, N_{def}). We characterize morphological instability using the dendrite length, $L_{\text{dendrite}} = x_{\text{tip}} - x_{\text{root}}$, where x_{tip} is the maximum x-position of the metal–electrolyte interface (the tip of the most advanced protrusion) and x_{root} is the minimum x-position (the deepest valley). The interface location is defined by the $\xi = 0.5$ contour. Fig. 2 presents benchmark fields for an initially flat Li–metal anode with $N_{\text{def}} = 5$ defects of amplitude $A_{\text{def}} = 0.15$ μm under an applied potential $\phi_a = -0.45$ V: (a–c) phase-field variable ξ, (d–f) Li-ion concentration $\tilde{c}_+$, and (g–i) electric potential ϕ, shown at $t = 20$ s, 60 s, and 100 s. At early time ($t = 20$ s), the interface remains nearly planar, and both $\tilde{c}_+$ and ϕ are approximately uniform along the transverse (y) direction, indicating weak lateral heterogeneity. As time increases, instability initiates at defect sites and progressively amplifies. By t = 60–100 s, pronounced

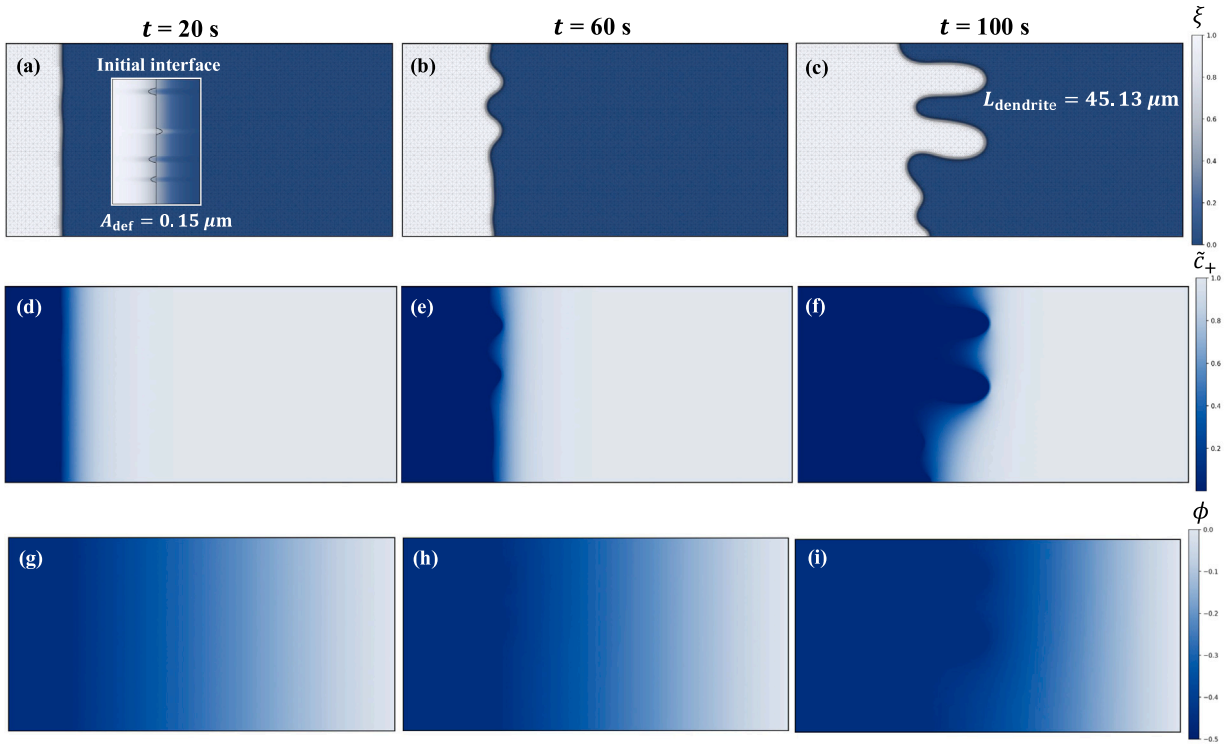

Fig. 2. Benchmark profiles of (a–c) phase-field variable $\xi(x, y)$, (d–f) Li-ion concentration $\tilde{c}_+(x, y)$, and (g–i) electric potential $\phi(x, y)$ for an initially flat Li–metal anode containing $N_{def} = 5$ defects with amplitude $A_{def} = 0.15$ μm. Snapshots are shown at $t = 20$ s, 60 s, and 100 s under an applied potential $\phi_a = -0.45$ V. At $t = 100$ s, the dendrite length reaches $L_{dendrite} = 45.13$ μm.

protrusions have formed, accompanied by elevated $\tilde{c}_+$ and ϕ near dendrite tips and reduced values in valleys. This redistribution of $\tilde{c}_+$ and ϕ reflects enhanced ionic flux toward protrusions and limited mass transport near the roots. These trends are consistent with previously reported phase-field simulations of electrochemical deposition [20] and provide a baseline reference for assessing the effects of nanoscale roughness and defect morphology in the following sections.

To compare our numerical results with theoretical predictions, we use the linear stability analysis developed in Ref. [29] under the same electrochemical parameters. The linear stability analysis yields a dispersion relation giving the growth rate w as a function of wavenumber k. In that framework, the variables are nondimensionalized as $\tilde{k} = kL_x$, $\tilde{w} = L_x^2 w/D_l$, and the analysis predicts a critical wavenumber $\tilde{k}_{cri}$ above which the interface is linearly stable. The nondimensional wavenumber $\tilde{k}$ is linked to the background wavelength in our nonlinear simulations through

$$\lambda_{bg} = \frac{2\pi(L_x - x_0)}{\tilde{k}}, \tag{24}$$

where L_x is the domain width and x_0 is the initial Li–metal thickness. We consider three background wavelengths, $\lambda_{bg} = 12.5$ μm, 0.5 μm, and 0.33 μm, corresponding to nondimensional wavenumbers $\tilde{k} = 90.5$, 2261, and 3393, respectively. The longest wavelength lies well within the unstable band ($\tilde{k} < \tilde{k}_{cri}$), whereas the two shorter wavelengths lie near and above the critical wavenumber. For each λ_{bg}, we perform nonlinear phase-field simulations with background amplitude $A_{bg} = 0.30$ μm and $N_{def} = 15$ defects of amplitude $A_{def} = 0.10$ μm superimposed on the interface.

Fig. 3 compares the linear stability analysis dispersion relation with phase-field variable snapshots at $t = 20$ s under an applied potential $\phi_a = -0.45$ V. For the long-wavelength background ($\lambda_{bg} = 12.5$ μm, $\tilde{k} = 90.5$), the interface already exhibits clear roughening and the onset of protrusions emerging from defect locations. In contrast, for the shorter-wavelength cases ($\lambda_{bg} = 0.5$ and 0.33 μm, $\tilde{k} = 2261$ and 3393), the interface remains nearly flat at the same time, with only small, defect-scale perturbations. This behavior is consistent with the dispersion relation: modes with $\tilde{k} < \tilde{k}_{cri}$ have positive growth rates and amplify rapidly, while modes with $\tilde{k} > \tilde{k}_{cri}$ are linearly stable. Fig. 4 shows the corresponding comparison at $t = 70$ s. For $\lambda_{bg} = 12.5$ μm, the initially unstable perturbations have grown into pronounced dendritic protrusions that extend deeply into the electrolyte, indicating continued amplification of the unstable mode. By contrast, for $\lambda_{bg} = 0.5$ and 0.33 μm, the interface remains relatively flat and the morphology is dominated by localized growth around individual defects; no large-scale corrugation develops at the background wavelength. Thus, even at later times, modes with $\tilde{k} > \tilde{k}_{cri}$ remain effectively suppressed in the nonlinear simulations, whereas modes in the unstable band continue to grow.

These comparisons highlight the strengths and limitations of the linear stability theory. The linear theory assumes infinitesimal perturbations on a defect-free, perfectly flat interface and does not account for finite background amplitude A_{bg}, discrete defects, or mode interactions as the morphology develops. As a result, linear stability analysis correctly predicts the existence of a critical wavenumber and captures the early-time selection between stable and unstable wavelength modes, but it cannot describe how roughness amplitude and defect statistics influence the subsequent nonlinear growth of dendrites. Our nonlinear phase-field simulations extend this framework by explicitly resolving finite-amplitude interface perturbations and defect-driven dynamics.

Next, we examine the influence of nanoscale surface roughness by varying the background wavelength λ_{bg} while keeping the roughness amplitude fixed. Fig. 5 shows the phase-field variable $\xi(x, y)$ for cases with identical defect configurations but different background roughness wavelengths, prescribed using $N_{bg} = 3, 8, 20$, and 200 complete surface waves. These correspond to wavelengths $\lambda_{bg} = 33.3$ μm, 12.5 μm, 5 μm, and 0.5 μm, respectively, all with the same amplitude $A_{bg} = 0.15$ μm. Each simulation includes $N_{def} = 5$ defects with amplitude $A_{def} = 0.15$ μm, and the interface morphology is shown at $t = 100$ s.

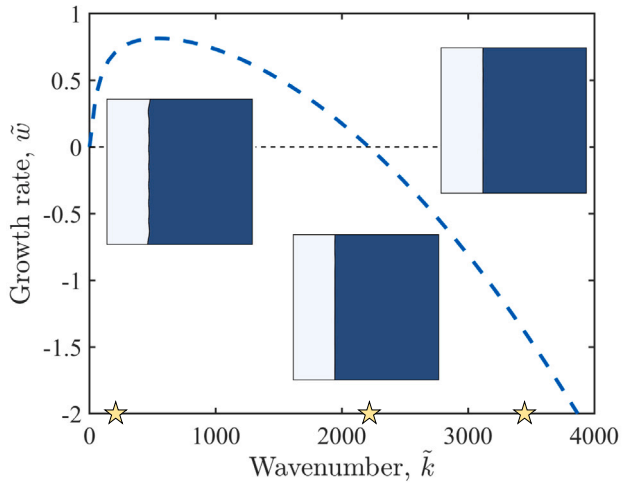

Fig. 3. Comparison between nonlinear simulations and linear stability analysis at early time, $t = 20$ s under an applied potential $\phi_a = -0.45$ V. Snapshots of the phase-field distribution $\xi(x, y)$ are embedded within the dispersion relation, which plots the nondimensional growth rate $\tilde{w}$ as a function of wavenumber $\tilde{k}$. Yellow star markers indicate the $\tilde{k}$ values corresponding to background wavelengths λ_{bg} = 12.5 μm, 0.5 μm, and 0.33 μm (i.e., $\tilde{k}$ = 90.5, 2261, and 3393). The phase-field snapshots correspond to simulations prescribed with these respective background wavelengths at amplitude $A_{bg} = 0.30$ μm, each containing $N_{def} = 15$ defects of amplitude $A_{def} = 0.10$ μm. For the longest wavelength ($\lambda_{bg} = 12.5$ μm), interfacial instability has already emerged, whereas the shorter-wavelength cases ($\lambda_{bg} = 0.5$ and 0.33 μm) remain nearly flat at this early time, consistent with linear stability analysis predictions.

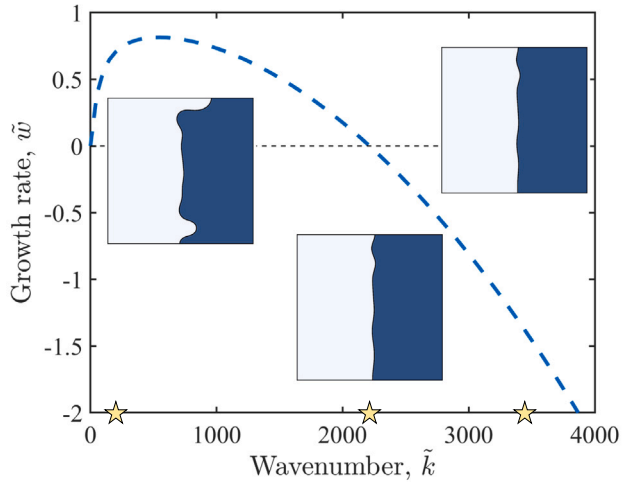

Fig. 4. Comparison between nonlinear simulations and linear stability analysis at later time, $t = 70$ s under an applied potential $\phi_a = -0.45$ V. Snapshots of the phase-field distribution $\xi(x, y)$ are embedded within the linear stability analysis dispersion relation, which plots the nondimensional growth rate $\tilde{w}$ as a function of wavenumber $\tilde{k}$. Vertical markers indicate the $\tilde{k}$ values corresponding to background wavelengths λ_{bg} = 12.5 μm, 0.5 μm, and 0.33 μm (i.e., $\tilde{k}$ = 90.5, 2261, and 3393). The phase-field snapshots correspond to simulations prescribed with these respective background wavelengths at amplitude A_{bg} = 0.30 μm, each containing $N_{def} = 15$ defects of amplitude $A_{def} = 0.10$ μm. For the long-wavelength case ($\lambda_{bg} = 12.5$ μm), the initially unstable perturbations have grown into pronounced dendritic protrusions, whereas the short-wavelength cases (λ_{bg} = 0.5 and 0.33 μm) remain relatively flat and defect-dominated, consistent with linear stability analysis predictions for $\tilde{k} > \tilde{k}_{cri}$.

For the largest wavelength, $\lambda_{bg} = 33.3$ μm, the dendrite length reaches $L_{dendrite} = 52.09$ μm, exceeding that of the flat reference case (Fig. 2, $L_{dendrite} = 45.13$ μm). This indicates that long-wavelength roughness amplifies interfacial instability.

As the background wavelength decreases from 33.3 μm to 12.5 μm, the dendrite length remains comparable to the benchmark case ($L_{dendrite} = 42.35$ μm). However, when the background wavelength is further reduced to 5 μm, dendrite growth is significantly suppressed, with the dendrite length decreasing to 26.03 μm. At $\lambda_{bg} = 5$ μm, the dendrite length becomes substantially smaller than that of the flat-interface benchmark, indicating strong stabilization induced by short-wavelength roughness. Further decreasing the wavelength to λ_{bg} = 0.5 μm does not yield additional stabilization ($L_{dendrite} = 28.95$ μm). This saturation behavior indicates the existence of a threshold wavelength below which further reduction in λ_{bg} no longer significantly enhances stability. In this regime, the background roughness is effectively smoothed out, and the late-stage morphology becomes dominated by defect-driven growth rather than by the imposed wavelength.

These results demonstrate that decreasing the roughness wavelength suppresses dendrite growth by increasing the surface-energy penalty associated with sharp protrusions, but only down to a finite cutoff scale. Below this threshold, interfacial evolution is governed primarily by defect statistics rather than background roughness, motivating further analysis of how stability depends jointly on λ_{bg}, A_{bg}, and defect characteristics.

We next examine how the background roughness amplitude A_{bg} modulates interfacial stability at different roughness wavelengths, while keeping the defect parameters fixed ($N_{def} = 5$, $A_{def} = 0.15$ μm). Fig. 6 compares two representative wavelengths: an intermediate wavelength case ($N_{bg} = 20$, $\lambda_{bg} = 5$ μm) and a high-frequency case (N_{bg} = 200, $\lambda_{bg} = 0.5$ μm), evaluated at $t = 100$ s under $\phi_a = -0.45$ V. For λ_{bg} = 5 μm (Fig. 6a–c), increasing the background amplitude from A_{bg} = 0.15 μm to 0.30 μm leads to nearly identical interface morphologies and very similar dendrite lengths ($L_{dendrite} = 26.03$ μm and 25.78 μm, respectively). However, when the amplitude is further increased to A_{bg} = 0.60 μm, the behavior changes qualitatively. The background roughness itself becomes unstable and begins to actively participate in the growth process. As a result, the interface develops stronger corrugations and the dendrite length increases markedly to 40.47 μm. Physically, at this intermediate wavelength, a sufficiently large roughness amplitude enhances local transport limitations and promotes current focusing along the background undulations, which weakens the stabilizing effect of surface energy and enables faster protrusion growth. In contrast, for the short-wavelength case λ_{bg} = 0.5 μm (Fig. 6d–f), increasing A_{bg} has only a minor influence on the interfacial morphology. The interface remains relatively smooth across the entire amplitude range, and the dendrite length varies only slightly, $L_{dendrite}$ = 28.95 μm, 28.26 μm, and 27.65 μm for A_{bg} = 0.15, 0.30, and 0.60 μm, respectively. This indicates that when the background wavelength is sufficiently small, the stabilizing effect of high-curvature roughness suppresses the amplification of the background mode, even at relatively large amplitudes, leaving only localized defect-scale growth.

Together, these results show that λ_{bg} and A_{bg} cannot be tuned independently. At intermediate (or long) wavelengths, increasing A_{bg} can push the background roughness into an unstable regime and significantly accelerate dendrite propagation. By contrast, at sufficiently short wavelengths, the background mode remains effectively stabilized and changes in A_{bg} have limited impact on $L_{dendrite}$. This coupled dependence highlights a practical design principle: when larger roughness amplitudes are unavoidable (e.g., due to fabrication limits), stability can be preserved by shifting the surface texture toward shorter wavelengths.

We next examine how defect amplitude A_{def} influences dendrite evolution, and how this effect depends on the background roughness amplitude A_{bg} at a fixed background wavelength $\lambda_{bg} = 12.5$ μm (N_{bg} = 8). Fig. 7 shows phase-field snapshots at $t = 100$ s for cases with N_{def} =

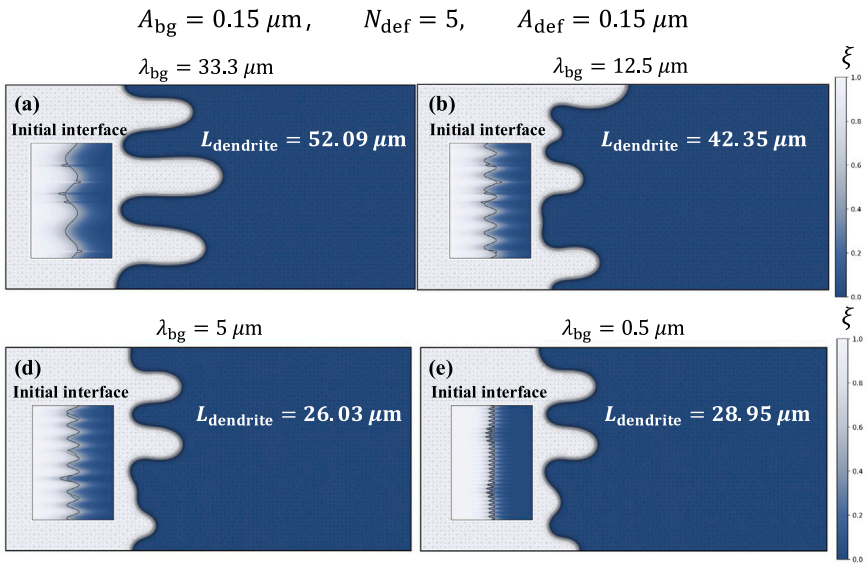

Fig. 5. Phase-field profiles $\xi(x, y)$ at $t = 100$ s under an applied potential $\phi_a = -0.45$ V for interfaces with identical defect configurations but varying background roughness wavelengths. All cases use a fixed background amplitude $A_{bg} = 0.15$ μm and $N_{def} = 5$ defects with amplitude $A_{def} = 0.15$ μm. The background wavelength decreases from (a) $\lambda_{bg} = 33.3$ μm, (b) 12.5 μm, (c) 5 μm, to (d) 0.5 μm. The corresponding dendrite lengths are $L_{dendrite} = 52.09$, 42.35, 26.03, and 28.95 μm, respectively. Insets show the initial interface morphology highlighting the imposed background roughness. The results demonstrate progressive stabilization with decreasing wavelength, followed by saturation below a critical roughness scale.

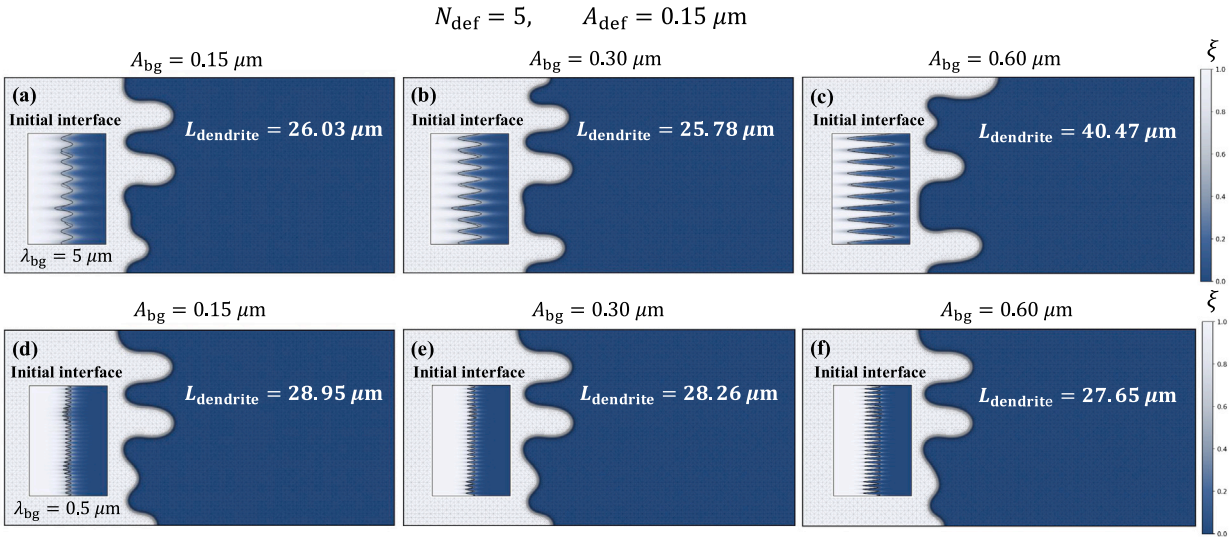

Fig. 6. Phase-field variable $\xi(x, y)$ profiles at $t = 100$ s under an applied potential $\phi_a = -0.45$ V for cases with identical defects but varying background nanoscale roughness amplitude. The roughness is prescribed using wavelengths (a–c) $\lambda_{bg} = 5$ μm, and (d–f) 0.5 μm at defect number $N_{def} = 5$ and defect amplitude $A_{def} = 0.15$ μm. The background amplitude is varied as $A_{bg} = 0.15$ μm, 0.30 μm, and 0.60 μm. For $\lambda_{bg} = 5$ μm, the corresponding dendrite lengths are $L_{dendrite} = 26.03$ μm, 25.78 μm, and 40.47 μm, showing a transition to unstable growth at large amplitude. For $\lambda_{bg} = 0.5$ μm, the dendrite length remains nearly unchanged ($L_{dendrite} = 28.95$, 28.26, and 27.65 μm), indicating that sufficiently short-wavelength roughness suppresses background-driven instability even at high amplitudes.

5 defects while varying A_{def}. For the larger background amplitude $A_{bg} = 0.15$ μm (Fig. 7a–c), the dependence on A_{def} is non-monotonic. Increasing A_{def} from 0.15 to 0.30 μm reduces the dendrite length from $L_{dendrite} = 42.35$ μm to 35.06 μm, indicating that intermediate defects can partially suppress the net longitudinal growth. In this regime, the background mode is already unstable, and moderate defects disrupt the coherent amplification of the long-wavelength corrugation, leading to a less extended growth front. However, when A_{def} is further increased to 0.60 μm, defects become dominant nucleation sites and drive strongly localized protrusion growth, causing $L_{dendrite}$ to increase to 53.36 μm. In contrast, for the smaller background amplitude $A_{bg} = 0.05$ μm (Fig. 7d–f), the dependence becomes monotonic: $L_{dendrite}$ increases from 29.83 μm to 40.23 μm and 57.12 μm as A_{def} rises from 0.15 to 0.30 and 0.60 μm. Here, increasing A_{def} primarily strengthens defect-driven current focusing and transport limitation, leading to progressively more severe dendritic growth.

These results demonstrate that the impact of defects cannot be interpreted independently of the imposed background morphology. At fixed λ_{bg}, A_{bg} sets whether the background roughness stabilizes or destabilizes the interface. Within that regime, A_{def} controls whether defects merely perturb the background evolution (intermediate A_{def}) or

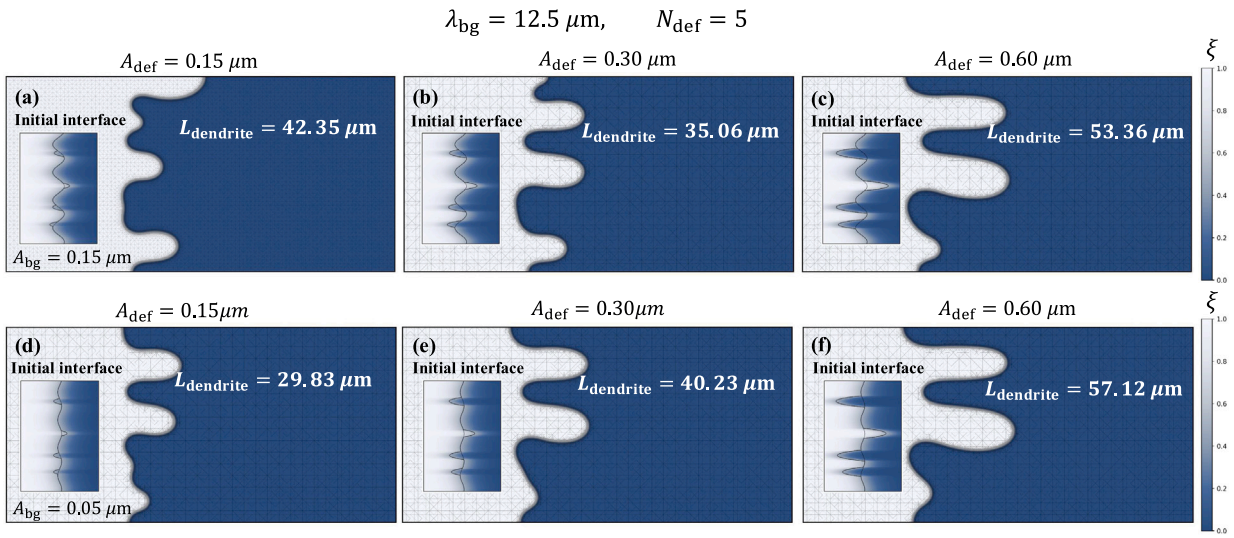

Fig. 7. Phase-field variable $\xi(x, y)$ profiles at $t = 100$ s for cases with varying defect amplitude and background roughness amplitude. The roughness is prescribed with wavelength $\lambda_{bg} = 12.5$ μm. Each case includes $N_{def} = 5$ defects. The defect amplitude is varied as $A_{def} = 0.15$, 0.30, and 0.60 μm. (a–c) $A_{bg} = 0.15$ μm with corresponding dendrite lengths $L_{dendrite} = 42.35$ μm, 35.06 μm, and 53.36 μm; (d–f) $A_{bg} = 0.05$ μm cases, with corresponding lengths $L_{dendrite} = 29.83$ μm, 40.23 μm, and 57.12 μm.

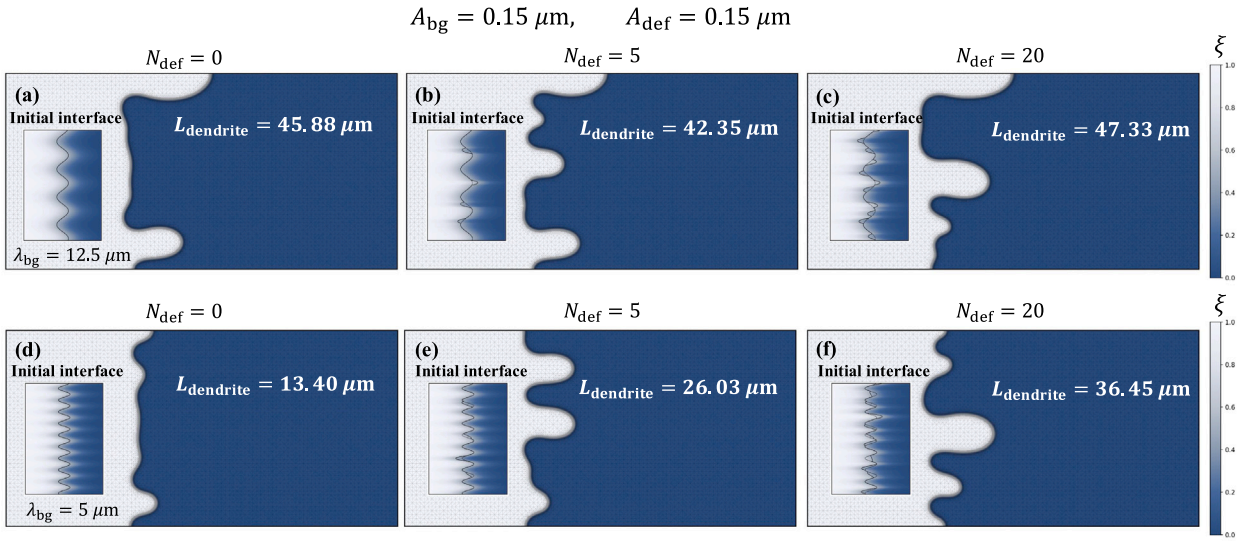

Fig. 8. Phase-field variable $\xi(x, y)$ profiles for cases with identical background roughness amplitude $A_{bg} = 0.15$ μm and defect amplitude $A_{def} = 0.15$ μm but varying background roughness wavelength and defect number. The number of defects increases across columns: $N_{def} = 0$ (no defects), $N_{def} = 5$, and $N_{def} = 20$. (a–c) $\lambda_{bg} = 12.5$ μm, with $L_{dendrite} = 45.88$ μm, 42.35 μm, and 47.33 μm; (d–f) $\lambda_{bg} = 5$ μm, with $L_{dendrite} = 13.40$ μm, 26.03 μm, and 36.45 μm.

dominate the morphology (large A_{def}). These results establish that interfacial evolution is governed by a coupled design space (λ_{bg}, A_{bg}, A_{def}) rather than any single parameter in isolation.

Finally, Fig. 8 examines the effect of defect number density by varying the number of discrete defects N_{def} while holding the background roughness amplitude and defect amplitude fixed ($A_{bg} = 0.15$ μm, $A_{def} = 0.15$ μm). We compare a low-frequency background (Fig. 8a–c, $\lambda_{bg} = 12.5$ μm) and a high-frequency background (Fig. 8d–f, $\lambda_{bg} = 5$ μm). In the low-frequency regime (Fig. 8a–c), the dependence on N_{def} is non-monotonic. In the defect-free case ($N_{def} = 0$), growth is primarily governed by the long-wavelength background corrugation, yielding $L_{dendrite} = 45.88$ μm. Introducing a small number of defects ($N_{def} = 5$) reduces the dendrite length to $L_{dendrite} = 42.35$ μm: the defects seed additional short-scale protrusions, which redistribute ionic flux and partially break up the coherent amplification of the long-wavelength background mode. However, when the defect density is further increased ($N_{def} = 20$), $L_{dendrite}$ increases to 47.33 μm. In the high-defect-density regime, closely spaced defects give rise to strong local current focusing and enhanced transport limitation, and thereby accelerating dendritic growth. In contrast, in the higher-frequency regime (Fig. 8d–f), increasing N_{def} produces a clear monotonic destabilization. Without defects ($N_{def} = 0$), the background roughness at $\lambda_{bg} = 5$ μm remains strongly stabilizing and dendrite growth is largely suppressed ($L_{dendrite} = 13.40$ μm). Adding defects introduces localized initiation sites that are not eliminated by the stabilizing background texture, increasing the dendrite length to 26.03 μm for $N_{def} = 5$ and to 36.45 μm for $N_{def} = 20$. Thus, in the high-frequency background regime, the interface remains relatively smooth without defects; however, as defect number increases, growth becomes progressively dominated by defect-induced protrusions.

Taken together, Fig. 8 demonstrates that the influence of defect density is strongly conditioned by the background wavelength. At

long wavelengths, a moderate number of defects can partially suppress dendrite growth by disrupting the dominant background mode, whereas excessive defect density reverses this effect by enhancing local current focusing. At shorter wavelengths, while dendrite growth is limited in the absence of defects, increasing defect density progressively increases the number of localized protrusions. These results reinforce that interfacial evolution is governed by a coupled parameter space ($\lambda_{bg}, A_{bg}, A_{def}, N_{def}$), rather than by any single descriptor of "roughness" or "defects" in isolation. While the simulations presented here are conducted under a fixed electrolyte composition, ion concentration, and applied potential in order to isolate geometric and defect-driven effects, the underlying physical mechanism is general. Electrochemical parameters such as electrolyte formulation, salt concentration, and applied voltage are expected to shift quantitative outcomes, such as dendrite length and the critical roughness wavelength, but do not alter the existence of a roughness-dependent stabilization regime or its coupled interaction with defect characteristics. In all cases, nonlinear interfacial evolution is governed by the same competition between surface-energy penalties, electrochemical driving forces, and ion-transport limitations.

4. Conclusions

We use nonlinear electrochemical phase-field simulations with adaptive spatial and temporal resolution to systematically investigate how nanoscale surface roughness and intrinsic defects jointly regulate Li–metal interfacial stability. By varying roughness wavelength (λ_{bg}) and amplitude (A_{bg}) while controlling defect amplitude (A_{def}) and number density (N_{def}), we establish a direct link between nanoscale geometry, defect characteristics, and the nonlinear evolution of Li deposition morphology. These simulations reveal several key findings that extend beyond what linear stability analysis or defect-free models can capture.

- The wavelength of nanoscale roughness plays a dominant role in determining stability. Decreasing λ_{bg} suppresses dendrite growth by increasing the surface-energy penalty associated with forming sharp protrusions. This stabilizing effect, however, saturates once λ_{bg} falls below a threshold set by the roughness amplitude and defect characteristics. Below this scale, further reduction in wavelength provides diminishing benefit, indicating the existence of an effective nanoscale cutoff that is only partially captured by linear stability theory.
- The roughness amplitude A_{bg} strongly modulates the stabilizing effect of λ_{bg}. For long-wavelength roughness, increasing A_{bg} destabilizes the interface by amplifying background corrugations and promoting current focusing, leading to accelerated dendrite growth. In contrast, in the short-wavelength regime the interface remains stable even as A_{bg} increases. These results demonstrate that λ_{bg} and A_{bg} are not independent design variables; rather, interfacial stability requires their joint optimization.
- The influence of defects depends strongly on whether the background roughness is stabilizing or destabilizing. At long wavelengths, a moderate number of defects can partially disrupt the dominant background mode and reduce dendrite extension. However, at sufficiently large defect amplitudes or densities, localized current focusing dominates and dendrite growth accelerates. In contrast, in the high-frequency regime, dendrite growth is limited in the absence of defects, increasing defect number progressively increases dendrite length as growth becomes increasingly governed by defect-induced protrusions.
- Comparison with linear stability analysis shows agreement in early-time behavior: linear theory correctly identifies the unstable wavelength range and the existence of a critical wavenumber. However, linear theory cannot account for finite-amplitude roughness, defect-driven transport localization, or the nonlinear competition between surface energy and electrochemical driving forces that govern late-stage morphology. The present simulations bridge this gap by revealing how nanoscale roughness and defect statistics jointly control the nonlinear evolution of Li deposition.

These results establish nanoscale roughness, rather than intrinsic defects alone, as a primary design parameter for stabilizing metal–electrolyte interfaces. Several practical design principles emerge. First, short-wavelength nanoscale roughness provides strong stabilization, even at moderate amplitudes. Second, long-wavelength nanoscale roughness can also stabilize the interface, but only when the amplitude is sufficiently small. Third, large-amplitude defects should be minimized or counteracted by intentionally introduced high-frequency roughness that suppresses long-wavelength instability and redistributes ionic flux away from defect sites. More broadly, interfacial evolution is governed by a coupled design space ($\lambda_{bg}, A_{bg}, A_{def}, N_{def}$) rather than by any single geometric or defect parameter in isolation.

Beyond interface-level morphology control, these nanoscale and microscale surface features can, in principle, be translated into effective transport descriptors, such as porosity and tortuosity, that enter macroscopic porous-electrode models [27,28]. Establishing such physically grounded constitutive relationships provides a pathway to incorporating interface morphology effects into continuum-scale predictions of voltage response and capacity fade.

The present framework establishes a foundation for predictive nanoscale interface design while also opening multiple directions for future work, including incorporating surface-energy anisotropy and coupling elastic–plastic deformation with SEI fracture. The parameter space explored here can be further expanded into machine-learning-assisted design maps, where surrogate models or neural operators accelerate the optimization of nanoscale roughness in the presence of defect distributions. Finally, extending the framework to three dimensions will be essential for capturing realistic dendrite pathways and practical failure modes. Integrating these directions will enable a comprehensive, predictive toolkit for designing next-generation Li–metal interfaces that remain stable under fast charging, high current densities, and long cycling lifetimes.

CRediT authorship contribution statement

Hongtao Sun: Writing – original draft, Visualization, Validation, Software, Methodology, Investigation, Formal analysis. **Weiyu Li:** Writing – review & editing, Supervision, Project administration, Methodology, Investigation, Funding acquisition, Conceptualization.

Declaration of competing interest

The authors declare that they have no known competing financial interests or personal relationships that could have appeared to influence the work reported in this paper.

Data availability

Data will be made available on request.

References

[1] J. Liu, Z. Bao, Y. Cui, E.J. Dufek, J.B. Goodenough, P. Khalifah, Q. Li, B.Y. Liaw, P. Liu, A. Manthiram, et al., Pathways for practical high-energy long-cycling lithium metal batteries, Nat. Energy 4 (3) (2019) 180–186.
[2] B. Liu, J.-G. Zhang, W. Xu, Advancing lithium metal batteries, Joule 2 (5) (2018) 833–845.
[3] L. He, Q. Sun, L. Lu, S. Adams, Understanding and preventing dendrite growth in lithium metal batteries, ACS Appl. Mater. Interfaces 13 (29) (2021) 34320–34331.
[4] X.-B. Cheng, R. Zhang, C.-Z. Zhao, Q. Zhang, Toward safe lithium metal anode in rechargeable batteries: a review, Chem. Rev. 117 (15) (2017) 10403–10473.

[5] X. Zhang, A. Wang, X. Liu, J. Luo, Dendrites in lithium metal anodes: suppression, regulation, and elimination, Acc. Chem. Res. 52 (11) (2019) 3223–3232.
[6] L. Frenck, G.K. Sethi, J.A. Maslyn, N.P. Balsara, Factors that control the formation of dendrites and other morphologies on lithium metal anodes, Front. Energy Res. 7 (2019) 115.
[7] F. Shi, A. Pei, A. Vailionis, J. Xie, B. Liu, J. Zhao, Y. Gong, Y. Cui, Strong texturing of lithium metal in batteries, Proc. Natl. Acad. Sci. 114 (46) (2017) 12138–12143.
[8] G. Qian, G. Zan, P. Pianetta, Y. Liu, Perspective—morphology and dynamics of metal dendrites in batteries revealed by X-ray computed tomography, J. Electrochem. Soc. 169 (12) (2023) 120540.
[9] H. Wang, Z. Yu, X. Kong, S.C. Kim, D.T. Boyle, J. Qin, Z. Bao, Y. Cui, Liquid electrolyte: The nexus of practical lithium metal batteries, Joule 6 (3) (2022) 588–616.
[10] S. Yuan, T. Kong, Y. Zhang, P. Dong, Y. Zhang, X. Dong, Y. Wang, Y. Xia, Advanced electrolyte design for high-energy-density Li-metal batteries under practical conditions, Angew. Chem. 133 (49) (2021) 25828–25842.
[11] Y. Rao, X. Li, S. Zhao, P. Liu, F. Wu, X. Liu, N. Zhou, S. Fang, S. Passerini, Fluorinated electrolyte formulations design enabling high-voltage and long-life lithium metal batteries, Nano Energy 123 (2024) 109362.
[12] P. Shi, L. Zhang, H. Xiang, X. Liang, Y. Sun, W. Xu, Lithium difluorophosphate as a dendrite-suppressing additive for lithium metal batteries, ACS Appl. Mater. Interfaces 10 (26) (2018) 22201–22209.
[13] J. Jiang, M. Li, X. Liu, J. Yi, Y. Jiang, C. Wu, H. Liu, B. Zhao, W. Li, X. Sun, J. Zhang, S. Dou, Multifunctional additives to realize dendrite-free lithium deposition in carbonate electrolytes toward low-temperature Li metal batteries, Adv. Energy Mater. 14 (27) (2024) 2400365.
[14] N.-W. Li, Y.-X. Yin, C.-P. Yang, Y.-G. Guo, An artificial solid electrolyte interphase layer for stable lithium metal anodes, Adv. Mater. 28 (9) (2016) 1853–1858.
[15] R. Xu, X.-B. Cheng, C. Yan, X.-Q. Zhang, Y. Xiao, C.-Z. Zhao, J.-Q. Huang, Q. Zhang, Artificial interphases for highly stable lithium metal anode, Matter 1 (2) (2019) 317–344.
[16] Y. Liu, Q. Liu, L. Xin, Y. Liu, F. Yang, E.A. Stach, J. Xie, Making Li-metal electrodes rechargeable by controlling the dendrite growth direction, Nat. Energy 2 (7) (2017) 1–10.
[17] C. Wei, H. Fei, Y. An, Y. Tao, J. Feng, Y. Qian, Uniform Li deposition by regulating the initial nucleation barrier via a simple liquid-metal coating for a dendrite-free Li–metal anode, J. Mater. Chem. A 7 (32) (2019) 18861–18870.
[18] Y. Sun, T. Yang, H. Ji, J. Zhou, Z. Wang, T. Qian, C. Yan, Boosting the optimization of lithium metal batteries by molecular dynamics simulations: A perspective, Adv. Energy Mater. 10 (41) (2020) 2002373.
[19] T.C. Lourenço, M. Ebadi, D. Brandell, J.L. Da Silva, L.T. Costa, Interfacial structures in ionic liquid-based ternary electrolytes for lithium-metal batteries: a molecular dynamics study, J. Phys. Chem. B 124 (43) (2020) 9648–9657.
[20] Z. Hong, V. Viswanathan, Phase-field simulations of lithium dendrite growth with open-source software, ACS Energy Lett. 3 (7) (2018) 1737–1743.
[21] L. Chen, H.W. Zhang, L.Y. Liang, Z. Liu, Y. Qi, P. Lu, J. Chen, L.Q. Chen, Modulation of dendritic patterns during electrodeposition: A nonlinear phase-field model, J. Power Sources 300 (2015) 376–385.
[22] Z. Hong, V. Viswanathan, Prospect of thermal shock induced healing of lithium dendrite, ACS Energy Lett. 4 (2019) 1012–1019.
[23] D. Qiao, X. Liu, R. Dou, Z. Wen, W. Zhou, L. Liu, Quantitative analysis of the inhibition effect of rising temperature and pulse charging on lithium dendrite growth, J. Energy Storage 49 (2022).
[24] H. Lee, N. Sitapure, S. Hwang, J.S.-I. Kwon, Multiscale modeling of dendrite formation in lithium-ion batteries, Comput. Chem. Eng. 153 (2021) 107415.
[25] B.G. Choobar, H. Modarress, R. Halladj, S. Amjad-Iranagh, Electrodeposition of lithium metal on lithium anode surface, a simulation study by: Kinetic Monte Carlo-embedded atom method, Comput. Mater. Sci. 192 (2021) 110343.
[26] G. Qi, X. Liu, X. Yi, R. Dou, Z. Wen, W. Zhou, L. Liu, Electrochemical-mechanical coupled phase-field modeling for lithium dendrite growth in all-solid-state lithium metal batteries, J. Energy Chem. 110 (2025) 80–87.
[27] F. Boso, W. Li, K. Um, D.M. Tartakovsky, Impact of carbon binder domain on the performance of lithium-metal batteries, J. Electrochem. Soc. 169 (10) (2022) 100550.
[28] X. Yang, W. Li, K. Um, D.M. Tartakovsky, Non-equilibrium thermal models of lithium batteries, J. Power Sources 623 (2024) 235428.
[29] W. Li, H.A. Tchelepi, Y. Ju, D.M. Tartakovsky, Stability-guided strategies to mitigate dendritic growth in lithium-metal batteries, J. Electrochem. Soc. 169 (6) (2022) 060536.
[30] W. Li, H.A. Tchelepi, D.M. Tartakovsky, Screening of electrolyte-anode buffers to suppress lithium dendrite growth in all-solid-state batteries, J. Electrochem. Soc. 170 (5) (2023) 050510.
[31] S.-K. Jung, I. Hwang, D. Chang, K.-Y. Park, S.J. Kim, W.M. Seong, D. Eum, J. Park, B. Kim, J. Kim, et al., Nanoscale phenomena in lithium-ion batteries, Chem. Rev. 120 (14) (2019) 6684–6737.
[32] G. Qian, G. Zan, J. Li, S.-J. Lee, Y. Wang, Y. Zhu, S. Gul, D.J. Vine, S. Lewis, W. Yun, Z.-F. Ma, P. Pianetta, J.-S.L. Lee, L. Li, Y. Liu, Structural, dynamic, and chemical complexities in zinc anode of an operating aqueous Zn-ion battery, Adv. Energy Mater. 12 (21) (2022) 2200255.
[33] J. Park, D. Kim, D. Jin, C. Phatak, K.Y. Cho, Y.-G. Lee, S. Hong, M.-H. Ryou, Y.M. Lee, Size effects of micro-pattern on lithium metal surface on the electrochemical performance of lithium metal secondary batteries, J. Power Sources 408 (2018) 136–142.
[34] C.P. Nielsen, H. Bruus, Morphological instability during steady electrodeposition at overlimiting currents, Phys. Rev. E 92 (5) (2015) 052310.
[35] A. Aryanfar, A. Tayyar, W.A. Goddard III, Controlling the roughening of growing electrochemical interfaces using temperature gradients, Phys. Rev. E 111 (1) (2025) 015505.
[36] J. Park, J. Jeong, Y. Lee, M. Oh, M.-H. Ryou, Y.M. Lee, Micro-patterned lithium metal anodes with suppressed dendrite formation for post lithium-ion batteries, Adv. Mater. Interfaces 3 (11) (2016) 1600140.
[37] T. Jang, J.-H. Kang, S. Kim, M. Shim, J. Lee, J. Song, W. Kim, K. Ryu, H.R. Byon, Nanometer-scale surface roughness of a 3-D Cu substrate promoting Li nucleation in Li-metal batteries, ACS Appl. Energy Mater. 4 (3) (2021) 2644–2651.
[38] X. Wang, Z. Chen, K. Jiang, M. Chen, S. Passerini, 3D host design strategies guiding "bottom–up" lithium deposition: a review, Adv. Energy Mater. 14 (19) (2024) 2304229.
[39] X. He, K. Zhang, Z. Zhu, Z. Tong, X. Liang, 3D-hosted lithium metal anodes, Chem. Soc. Rev. 53 (1) (2024) 9–24.
[40] Y. Li, Y. Wang, B. Chen, Y. Lin, G. Zhang, M. Avdeev, S. Shi, Proactive lithium dendrite regulation enabled by manipulating separator microstructure using high-fidelity phase-field simulation, Adv. Energy Mater. 15 (2025).
[41] W. Li, W. Korbitz, H.A. Tchelepi, A. Tran, SEI-electrolyte dyads for dendrite suppression in Li-Metal batteries, J. Electrochem. Soc. 172 (7) (2025) 070524.
[42] N. Provatas, N. Goldenfeld, J. Dantzig, Efficient computation of dendritic microstructures using adaptive mesh refinement, Phys. Rev. Lett. 80 (15) (1998) 3308.
[43] S. Sakane, T. Takaki, T. Aoki, Parallel-GPU-accelerated adaptive mesh refinement for three-dimensional phase-field simulation of dendritic growth during solidification of binary alloy, Mater. Theory 6 (1) (2022) 3.
[44] Z. Mu, Z. Guo, Y.-H. Lin, Simulation of 3-D lithium dendritic evolution under multiple electrochemical states: A parallel phase field approach, Energy Storage Mater. 30 (2020) 52–58.
[45] Q. Chen, K. Geng, K. Sieradzki, Prospects for dendrite-free cycling of Li metal batteries, J. Electrochem. Soc. 162 (10) (2015) A2004.
[46] I. Lindsey, C. Mondl, X. Meng, In-situ and operando microscopy studies on lithium metal anodes: A review, Energy Adv. (2025).
[47] W. Li, Onset of lithium plating in fast-charging Li-ion batteries, ACS Energy Lett. 10 (2025) 1596–1604.
[48] L.-Q. Chen, Phase-field models for microstructure evolution, Annu. Rev. Mater. Res. 32 (1) (2002) 113–140.
[49] D.A. Cogswell, Quantitative phase-field modeling of dendritic electrodeposition, Phys. Rev. E 92 (2015).
[50] J. Jeon, G.H. Yoon, T. Vegge, J.H. Chang, Phase-field investigation of lithium electrodeposition at different applied overpotentials and operating temperatures, ACS Appl. Mater. Interfaces 14 (2022) 15275–15286.
[51] M.E. Arguello, N.A. Labanda, V.M. Calo, M. Gumulya, R. Utikar, J. Derksen, Dendrite formation in rechargeable lithium-metal batteries: Phase-field modeling using open-source finite element library, J. Energy Storage 53 (2022).
[52] H. Wang, H. Gao, X. Chen, J. Zhu, W. Li, Z. Gong, Y. Li, M.S. Wang, Y. Yang, Linking the defects to the formation and growth of Li dendrite in all-solid-state batteries, Adv. Energy Mater. 11 (2021).
[53] M. Alnæs, J. Blechta, J. Hake, A. Johansson, B. Kehlet, A. Logg, C. Richardson, J. Ring, M.E. Rognes, G.N. Wells, The FEniCS project version 1.5, Archive Numer. Software 3 (100) (2015).

Hongtao Sun is a Ph.D. student in the Department of Mechanical Engineering at the University of Wisconsin–Madison, advised by Prof. Weiyu Li. He received his B.S. and M.S. degrees from Hunan University. His research focuses on computational modeling of electrochemical systems, with an emphasis on phase-field simulations of lithium metal deposition, interfacial instability, and nanoscale transport phenomena in energy storage materials.

Weiyu Li is an Alfred Fritz Assistant Professor in the Department of Mechanical Engineering at the University of Wisconsin–Madison, where she leads the Li's Energy and Sustainability Solutions (LESS) Lab. Her research develops multiphysics and multiscale modeling frameworks to advance sustainability in energy storage, water resources, and human health. Li received her Ph.D. in Energy Science and Engineering from Stanford University in 2023. Li is the sole recipient of the Siebel Scholars Award in Energy Science, class of 2023. She has also received Henry J. Ramey Fellowship Award at Stanford University, and the Princeton University Fellowship in Natural Sciences and Engineering.